Grain structure and magnetic relaxation of self-assembled Co nanowires

2013 J. Phys.: Condens. Matter 25 056002

(http://iopscience.iop.org/0953-8984/25/5/056002)

J. Phys.: Condens. Matter **25** (2013) 056002 (9pp) doi:10.1088/0953-8984/25/5/056002

Grain structure and magnetic relaxation of self-assembled Co nanowires

P Schio[1,2,5], F J Bonilla[1], Y Zheng[1,3], D Demaille[1], J Milano[1,3,4], A J A de Oliveira[2] and F Vidal[1,3]

[1] Institut des NanoSciences de Paris, UPMC, CNRS UMR 7588, 4 place Jussieu 75005 Paris, France
[2] Departamento de Física, UFSCar, C. P. 676, 13565-905 São Carlos, São Paulo, Brazil
[3] LIFAN, Laboratoire International Franco-Argentin en Nanosciences, Argentina and France
[4] CNEA-CONICET and Instituto Balseiro, UNCU, CAB (R8402AGP) San Carlos de Bariloche, RN, Argentina

E-mail: franck.vidal@insp.jussieu.fr

Received 21 September 2012, in final form 9 November 2012
Published 21 December 2012
Online at stacks.iop.org/JPhysCM/25/056002

Abstract
The magnetic relaxation of Co nanowires assemblies embedded in $CeO_2/SrTiO_3(001)$ epilayers has been investigated by magnetization decay measurements. Two different samples were studied, with nanowires having distinct crystallographic structures and diameters of 3 and 5 nm. The structure of the nanowires was derived from high-resolution transmission electron microscopy analysis. The 3 nm diameter nanowires are made of hcp Co grains with the *c*-axis pointing along one of the four ⟨111⟩ directions of the CeO_2 matrix, separated by fcc Co regions. In the 5 nm diameter nanowires, the grains are smaller and the density of stacking faults is much higher. The magnetic viscosity coefficient (S) of these two systems was measured as a function of the applied field and of the temperature. Analysis of the variation of S and of the activation volume for magnetization reversal reveals distinct behaviors for the two systems. In the nanowires assembly with 5 nm diameter, the results can be described by considering an energy barrier distribution related to shape anisotropy and are consistent with a thermally activated reversal of the magnetization. In contrast, the anomalous behavior of the 3 nm diameter wires indicates that additional sources of anisotropy have to be considered in order to describe the distribution of energy barriers and the reversal process. The distinct magnetic behaviors observed in these two systems can be rationalized by considering the grain structure of the nanowires and the resulting effective magnetocrystalline anisotropy.

(Some figures may appear in colour only in the online journal)

1. Introduction

Ferromagnetic nanowires (FNWs) have attracted considerable attention in the past decades. This interest lies in their potential applications in ultrahigh density magnetic storage devices. Also, from a more fundamental perspective, these objects offer an ideal testing ground in the field of nanomagnetism because their characteristic dimensions, i.e. their diameters, fall in the range of magnetic length scales such as the exchange length or the domain wall width. Thus, the issue of magnetization reversal in FNWs has been increasingly studied over recent years [1–4].

Most of the magnetic studies have been performed on FNWs assemblies grown by electrodeposition in porous templates. Such growth techniques have many advantages and allow one to obtain large and relatively ordered FNWs assemblies. However, decreasing the diameter of the wires below ∼5 nm with these pore-filling methods is not obvious. Another strategy to obtain FNWs assemblies with reduced diameters consists in using growth techniques relying on vertical self-assembly. Recent studies showed that it is indeed possible to obtain FNWs assemblies embedded in an oxide matrix using pulsed-laser deposition (PLD), as demonstrated

[5] Present address: Laboratório Nacional de Luz Síncrotron, Campinas, São Paulo 13083-970, CP 6192, Brazil.

in the case of Fe FNWs in a $LaSrFeO_4$ matrix [5] and $CoFe_2O_4$ FNWs in a $BaTiO_3$ matrix [6]. We have shown that it is possible to use PLD in order to obtain Co nanowires embedded in an epitaxial $CeO_2/SrTiO_3(001)$ matrix [7–10]. Analyzing the dependence of the coercive field in FNWs assemblies with 3 and 5 nm diameters, hereafter labeled as d_3 and d_5, we could show that the magnetization reversal occurs through a localized reversal mechanism [8]. In the d_5 sample, the magnetostatic contribution to the anisotropy was sufficient to explain the observed behavior. In contrast, the variation of the coercive field with the temperature could only be explained by considering a contribution of the magnetocrystalline anisotropy in d_3. We tentatively ascribed such distinct behavior of d_3 and d_5 to the grain structure of the wires. More recently, in the case of 3 nm wide nanowires, we could correlate the magnetic behavior with the structure of the wires [10]. In the present paper, we report on the study of the grain structure in d_3 and d_5 as derived from high-resolution electron microscopy and on magnetic viscosity measurements of the d_3 and d_5 Co FNWs assemblies.

This paper is organized as follows: in section 2, we briefly describe the experimental procedures used to obtain the d_3 and d_5 samples, to investigate the internal structure of the nanowires, and to measure their magnetic viscosity; in section 3, the results on the structure of the nanowires in d_3 and d_5 are presented; in section 4, the theoretical background necessary to the exploitation of magnetic viscosity measurements is detailed; and in section 5, the relaxation results are presented. Finally, the structural and magnetic results are discussed in section 6.

2. Experimental details

The growth technique used to obtain the d_3 and d_5 Co FNWs assemblies consists in sequential deposition of CoO and CeO_2 on $SrTiO_3(001)$ substrates by pulsed-laser deposition. An excimer laser (KrF) operating at 248 nm and 2 Hz was used. Before growing the embedded nanowires, a pure CeO_2 buffer with thickness 4 nm is deposited on $SrTiO_3(001)$ under 5.10^{-2} mbar of oxygen at 650 °C in order to ensure a good quality of the films with the desired epitaxial relationship [11]. The embedded wires film is grown subsequently at 650 °C under vacuum (at a pressure lower than 10^{-5} mbar) by shooting sequentially on the CoO and CeO_2 targets. Under the temperature and pressure conditions used, ceria reduces CoO into Co and the laser shot sequence can be adjusted in order to control the cobalt content of the films. As shown previously, such a method allows us to obtained self-assembled Co nanowires embedded in a $CeO_2/SrTiO_3(001)$ epilayer. Further details on the structure and composition of the samples studied here can be found in our previous paper [8].

High-resolution transmission electron microscopy (HRTEM) data were acquired using a JEOL JEM 2100F equipped with a field-emission gun operated at 200 kV. The cross-sections were prepared by ion milling. The data processing was performed using standard software (DigitalMicrograph and Image J).

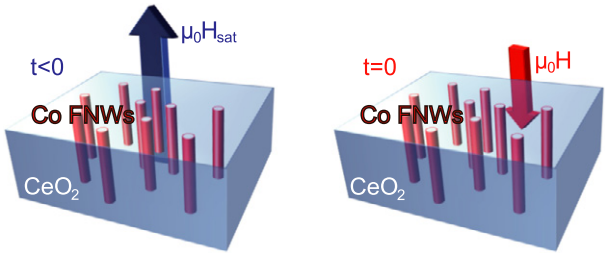

Figure 1. Principle of magnetic relaxation measurements performed on a ferromagnetic nanowires assembly embedded in CeO_2. After saturating the sample, the magnetic field is reversed at time $t = 0$ and the subsequent evolution of the magnetization is monitored as a function of time.

Magnetic measurements were performed in a superconducting quantum device (SQUID) magnetometer (Quantum Design MPMS—5S). Along with static measurements, the slow relaxation dynamics of the magnetization can be studied through so-called magnetic viscosity measurements [12, 13]. The measurements consist in monitoring the magnetization variation as a function of time after reversing the magnetic field, the sample being originally saturated as illustrated in figure 1. Such magnetic viscosity measurements have been used in order to probe the thermally activated reversal in ferromagnetic nanowires [4, 14–17]. For each experiment, the procedure used to measure the magnetic viscosity consists in: (i) saturating the sample with a high magnetic field (+2 T), (ii) switching the field to a given value between 0.1 and −0.9 T (the negative sign here means that the field is applied in the opposite sense with respect to the initial saturation field), (iii) monitoring the magnetization variation with time. For the measurements reported here the waiting time was 2400 s. These measurements were performed for the d_3 and d_5 assemblies as a function of the temperature in the 20–350 K range. The magnetic field was applied along the easy axis direction, corresponding to the direction of the wires axis which is parallel to the [001] direction of CeO_2 (growth direction).

3. Grain structure of the nanowires

The structure of the Co NWs was investigated using HRTEM. As the nanowires are embedded in the epitaxial CeO_2 matrix, the formation of cross-sectional images can involve multiple diffraction processes. A simple picture of such a phenomenon is the following: considering diffraction in the matrix as a first step, each diffracted beam can then be considered as a primary beam and may be diffracted in the NWs. Therefore, the diffraction patterns obtained in cross-section exhibit many additional spots with respect to the simple addition of the diffraction pattern of Co and CeO_2. These additional spots result from the convolution of the pattern of the matrix and the pattern of the embedded objects, as illustrated in figure 2.

Co can exist in the fcc and hcp structures. In bulk, the hcp structure is the stablest one at room temperature and the hcp–fcc transition occurs above 425 °C. In nanostructures, however, it is not uncommon to find Co in its fcc form at room

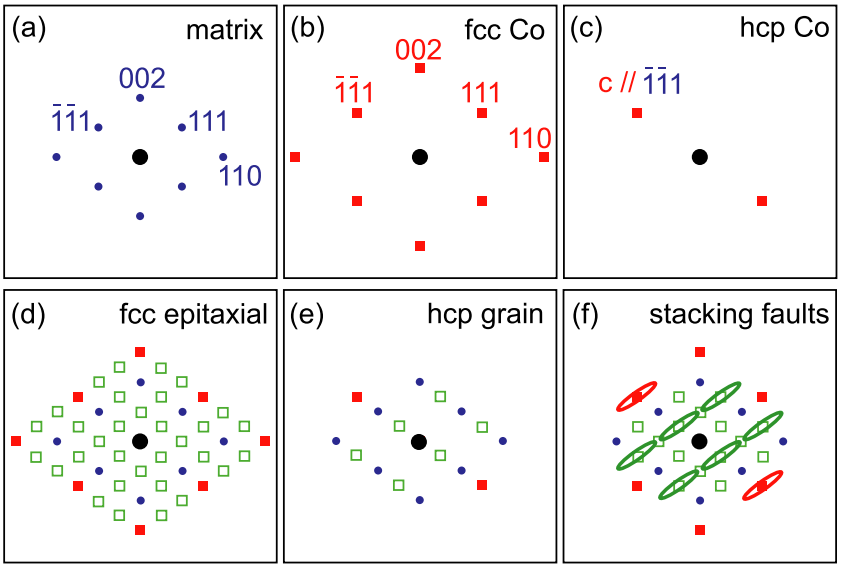

Figure 2. Schematics of the expected diffraction patterns of Co nanowires embedded in CeO_2 with a $[1\bar{1}0]$ zone axis. (a) Pattern for pure CeO_2. (b) Pattern for pure fcc Co aligned with CeO_2. (c) pattern for pure hcp Co with the *c*-axis parallel to the $[\bar{1}\bar{1}1]$ direction of CeO_2. (d) Diffraction pattern for epitaxial fcc Co nanowire in CeO_2, empty squares represent high-order diffraction spots. (e) Diffraction pattern for hcp Co nanowire in CeO_2 with the *c*-axis parallel to the $[\bar{1}\bar{1}1]$ direction of CeO_2, empty squares represent high-order diffraction spots. (f) Pattern for a system with stacking faults in the [111] direction.

temperature [18, 19], due to factors such as strain or interface energetic contributions.

In its fcc form, Co has a $a_{Co} = 3.54$ Å lattice parameter. The lattice parameter of CeO_2 (cubic fluorite structure) is $a_{ceria} = 5.41$ Å. Considering a cube-on-cube epitaxy of fcc Co and CeO_2, with $[001]_{Co} \parallel [001]_{ceria}$ and $[010]_{Co} \parallel [010]_{ceria}$, the lattice mismatch is large. However, considering 3 unit cells of Co for 2 unit cells of ceria ($3a_{Co} = 10.62$ Å, $2a_{ceria} = 10.82$ Å) reduces the lattice mismatch to a modest 2% value. Such epitaxy would lead to the observation of the diffraction pattern depicted in figure 2(d) in cross-section along the $[1\bar{1}0]$ zone axis of ceria. Such a pattern can be used as a fingerprint of cube-on-cube epitaxy of fcc Co and CeO_2.

Through the fcc to hcp phase transition, one of the [111] direction of fcc Co will transform into the [001] direction of the hcp phase (the *c*-axis). Considering as a starting point fcc Co aligned with ceria, the resulting hcp Co would have its *c*-axis parallel to one of the ⟨111⟩ directions of ceria. This would lead to the observation of a pattern similar to the one in figure 2(e) expected for *c* parallel to $[\bar{1}\bar{1}1]$. Such a pattern and its symmetric counterpart with respect to the [001] direction of the matrix can therefore be used as fingerprints of Co hcp grains with their *c*-axis lying along one of the ⟨111⟩ directions of the CeO_2 matrix.

During the fcc–hcp transition in the embedded wires, strain could be the source of defect formation in order to relax part of the elastic energy of the system. Among the possible defects, stacking faults along the ⟨111⟩ directions are very likely. With the case illustrated in figure 2(e) as a starting point, the formation of incommensurate stacking faults along [111] would induce the appearance of elongated spots in the diffraction pattern, as illustrated in figure 2(f).

Having established some possible fingerprints of fcc and hcp Co, we now turn to the analysis of HRTEM images acquired along the $[1\bar{1}0]$ zone axis for d_3 and d_5. Figure 3(a) shows the HRTEM image of a portion of NW embedded in CeO_2 acquired on the d_3 sample. The fast Fourier transform (FFT) of this image is given in the inset of figure 3(a), revealing a pattern identical to the one expected in the case of cube-on-cube epitaxy of fcc Co and CeO_2, figure 2(d). The lattice parameter deduced from analysis of the FFT pattern is $a_{Co} = 3.5 \pm 0.1$ Å in very good agreement with the expected value for fcc Co. This evidences the presence of epitaxial fcc Co grains within the nanowires of d_3. However, such fcc grains are not the major structure found in d_3. Detailed study of the wires structure reveals that most of the grains in d_3 are composed of hcp Co, such as the one shown in figure 3(b) that can be actually identified by comparison with the fingerprint pattern of figure 2(e). Such measurements were performed in different grains along a wire and this procedure was then repeated in distinct wires at several zones of the sample. This was done for 3 different pieces of sample. The picture that emerges from such measurements is the following: the nanowires in d_3 are made of hcp grains with their *c*-axis oriented along one of the ⟨111⟩ directions of the matrix (within ±3°), separated by fcc regions.

We performed a similar analysis of the structure of the wires in d_5. Compared to d_3, the grain structure of d_5 is much more disordered, with smaller hcp grains and frequent regions with a high density of stacking faults. This is exemplified in figure 4 showing a representative HRTEM image of the d_5 assembly. In the FFT pattern in figure 4, one can see the characteristic fingerprint of stacking faults as described in figure 2(f). Filtering this image on spots corresponding to a particular *c*-axis orientation or keeping only the intensity of a region characteristic of the stacking faults allows us to evidence (i) the reduced dimensions of the hcp grains

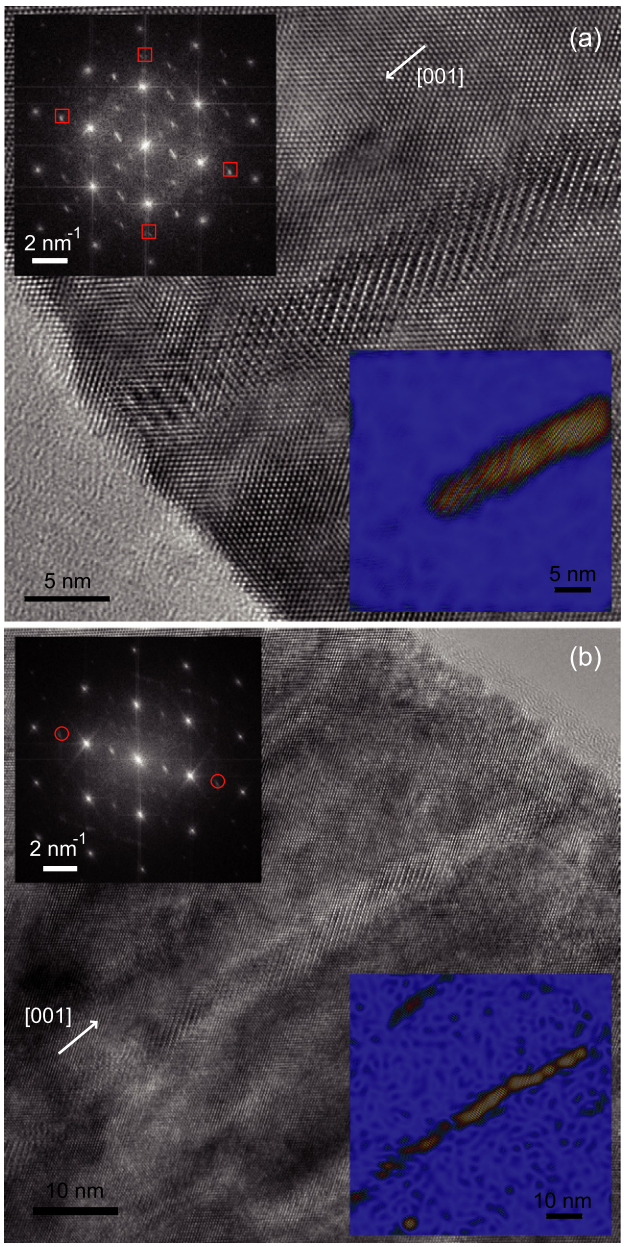

Figure 3. (a) HRTEM image of d_3 along the [1$\bar{1}$0] zone axis, showing a portion of nanowire made of fcc Co. Insets: FFT and filtered image taking only the fcc related spots indicated by squares in the FFT. (b) HRTEM image of d_3 along the [1$\bar{1}$0] zone axis, showing a portion of nanowire made of hcp Co. Insets: FFT and filtered image taking only the hcp related spots indicated by circles in the FFT.

compared to d_3 and (ii) the extension of the stacking faulted regions.

The results obtained on the structure of the wires can be summarized as follows: the Co wires have their long axis oriented along the growth direction that corresponds to the [001] direction of CeO_2. This [001] axis is the easy axis of the nanowires. The FNWs are made of hcp grains possibly separated by fcc regions. The fcc Co is epitaxied in the CeO_2 matrix. This is a cube-on-cube epitaxy with the unit cells of fcc Co and CeO_2 aligned. The hcp grains have their c-axis oriented along one of the ⟨111⟩ directions of the matrix. This is what is expected for a parent fcc Co phase in cube-on-cube epitaxy with ceria that would have transited to the hcp phase. Thus, the structures of the wires may form during the cooling step where initially epitaxial fcc Co transits towards the hcp phase. The result from such process is that the structure of the d_3 and d_5 samples differ. While d_3 is made of hcp grains extending through the whole diameter of the wires, the structure is much more disordered in d_5, with comparatively smaller grains and some regions with a high density of stacking faults.

4. Theoretical background on magnetic viscosity measurements

Following the Néel–Brown model [20, 21] that describes thermally activated relaxation of the magnetization over an energy barrier E_a, the relaxation time τ is given by an Arrhenius law:

$$\tau = \tau_0 \exp \frac{E_a}{k_B T}. \quad (1)$$

In this expression, τ_0 is the inverse of an attempt frequency of the order of 10^9 s^{-1}, T is the temperature, and k_B is the Boltzmann constant. In ideal systems composed of identical magnetic objects having the same activation energy, equation (1) would lead to an exponential decay of the magnetization with time following a reversal of the external magnetic field. Such behavior is rarely observed in real systems owing to structural inhomogeneities. Because of the dispersion inherent to real structure, there is not a single energy barrier to cross but instead a continuous distribution, $P(E_a)$. Averaging over such a distribution gives the following logarithmic law for the magnetization decay after H reversal at time t_0:

$$M(t) = M(t_0) - S(H, T) \ln(t/t_0) \quad (2)$$

where $S(H, T)$ is the magnetic viscosity coefficient [12, 13], which depends on the temperature and on the external magnetic field. The viscosity can be related to the distribution of barriers through the following relation [12]:

$$S = 2k_B T P(0) M_s. \quad (3)$$

Thus, S varies linearly with the temperature provided that M_s is constant and that the distribution of activation energies does not depend on the temperature. For a rectangular distribution of energy barriers of width ΔE_a, modeling a broad and smoothly varying distribution, it can be shown that [12]:

$$S = 2k_B T M_s / \Delta E_a. \quad (4)$$

It is also possible to extract valuable information on the localized or delocalized nature of the reversal by extracting from magnetic measurements the activation volume involved in the process. An activation volume smaller than the physical size of the magnetic system is a clear fingerprint of a localized reversal. This activation volume can be defined as [22]:

$$\mu_0 M_s V^\star = -\partial E_a / \partial H. \quad (5)$$

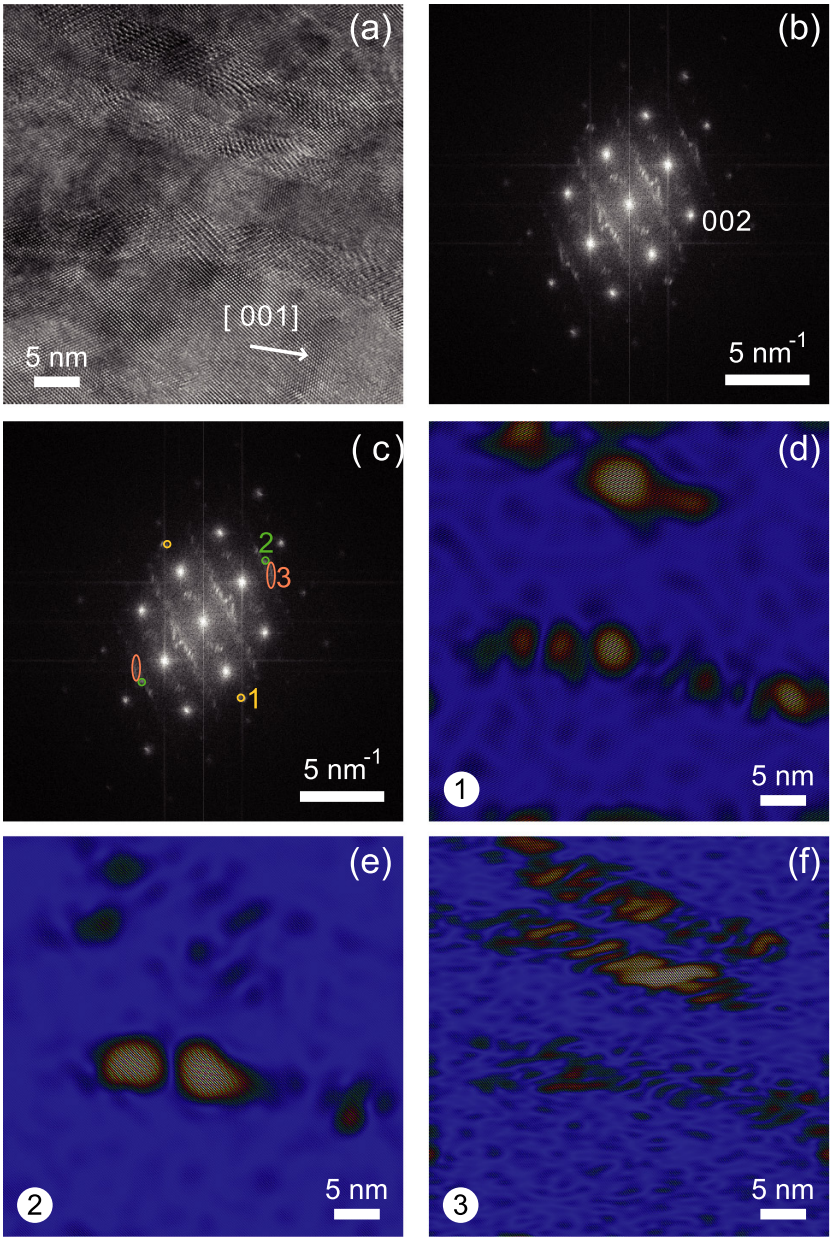

Figure 4. (a) HRTEM image of d_5 along $[1\bar{1}0]$. (b) FFT of (a). (c) Same as (b) with spots used for filtering in ((d)–(f)). (d) Filtered image using spots labeled 1 in (c). (e) Filtered image using spots labeled 2 in (c). (f) Filtered image using spots labeled 3 in (c).

The activation volume can be extracted from experiments measuring S and the irreversible part of the susceptibility χ_{irr}. Indeed, the magnetic viscosity can also be expressed as [13]:

$$S = -k_{\mathrm{B}}T\chi_{\mathrm{irr}}/(\partial E_{\mathrm{a}}/\partial H). \tag{6}$$

Therefore, using equations (5) and (6), the activation volume as a function of S and χ_{irr} reads:

$$V^{\star} = k_{\mathrm{B}}T\chi_{\mathrm{irr}}/\mu_0 M_s S. \tag{7}$$

The activation energy of reversal, E_{a}, depends on the applied magnetic field: if the field is sufficiently high then the magnetic moment can be reversed and E_{a} is overcome. This dependence of the activation energy on the external magnetic field is accounted for by the following phenomenological expression:

$$E_{\mathrm{a}}(H) = KV\left(1 - \frac{H}{H_0}\right)^m \tag{8}$$

where K is the magnetic anisotropy of the system, V is the switching volume, and $\mu_0 H_0 = 2K/M_s$, with M_s being the saturation magnetization. In the case of aligned spherical Stoner–Wohlfarth particles [23], the exponent is $m = 2$. This exponent is indeed valid for symmetric energy landscapes. For most magnetic systems having a real structure departing from such an ideal situation, such as polycrystalline nanowires for example, $m = 3/2$ [12, 24]. Combining equations (1) and (8) gives the dependence of the coercive field, $\mu_0 H_c$, on the

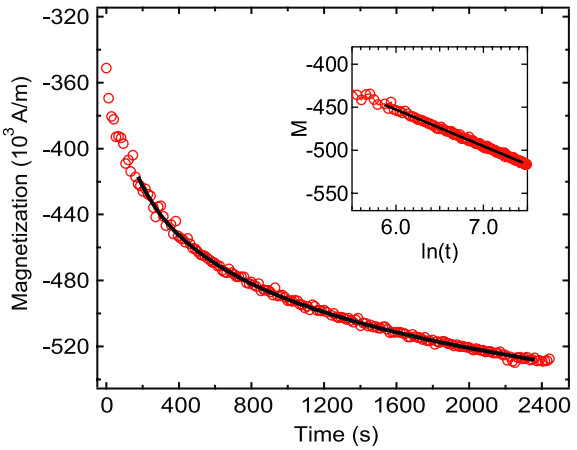

Figure 5. Typical measurement of time decay of the magnetization. The data have been obtained after reversing the field from 2 T to −0.1375 T on d_5 (temperature: 300 K). The black line is a logarithmic fit according to equation (2). Inset: magnetization decay plotted as a function of ln(t). The black line is a linear fit allowing for straightforward extraction of the magnetic viscosity parameter.

temperature [25]:

$$\mu_0 H_c = \mu_0 H_0 \left[1 - \left(\frac{k_B T \ln(\tau/\tau_0)}{KV}\right)^{1/m}\right]. \qquad (9)$$

Then, the following expression of $V^\star$ as a function of the temperature can be deduced:

$$V^\star = \frac{m}{2} V^{1/m} \left[\frac{k_B T}{K} \ln(\tau/\tau_0)\right]^{(m-1)/m}. \qquad (10)$$

Thus, experimental values of $V^\star$ extracted from magnetic viscosity measurements using equation (7) can be compared to equation (10).

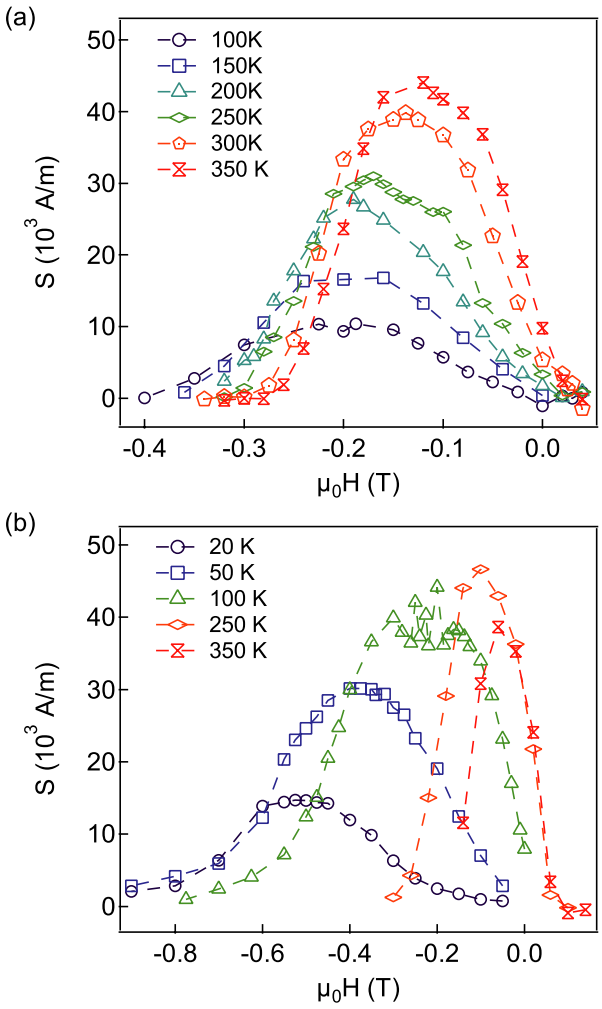

Figure 6. (a) Magnetic viscosity coefficients $S(H, T)$ of d_5 as a function of the applied field at various temperatures. (b) Same as (a) for the d_3 FNWs assembly.

5. Magnetic relaxation

Figure 5 shows the evolution of the magnetization of d_5 at 300 K as a function of time after saturating the sample in one sense (2 T) and subsequently applying a reverse field (−0.1375 T) at $t = 0$. Similar behaviors were obtained for both d_3 and d_5 samples over the range of applied fields and temperatures studied. In all cases, the decay of the magnetization could be satisfactorily fitted by a logarithmic decay following equation (2). The good agreement of the fit can be seen in figure 5, where $M(t)$ is plotted as a function of t and ln(t). From these measurements, the magnetic viscosity, $S(H, T)$ was obtained in a broad range of fields and temperature for d_3 and d_5. The results are summarized in figure 6, which shows the evolution of S as a function of the applied field for temperatures in the 20–350 K range.

At a given temperature, the $S(H)$ curve is a bell-shaped curve with a maximum located near the coercive field of the FNWs assembly. This can be understood by considering the dependence of energy barriers on the magnetic field. Considering an homogeneous system with a single energy barrier, it can be seen from equation (8) that the barrier for reversal is lowest when the applied field matches $\mu_0 H_0$. Now, considering a FNWs assembly that has a broad energy barriers distribution due to inhomogeneities, the coercive field is the field for which the highest proportion of barriers can be crossed. This explains the fact that the magnetic viscosity peaks at $\mu_0 H = \mu_0 H_c$. This is indeed verified, as shown in figures 7((a)–(b)), where the coercive field and the field of maximal viscosity ($\mu_0 H_{S\max}$) are plotted as a function of the temperature for d_3 and d_5. For the d_5 sample, the $S(H)$ curves gain in intensity and the position of their maximum shifts towards lower applied fields (in magnitude) as the temperature increases. This shift is consistent with the evolution of $\mu_0 H_c$ reported previously [8].

The evolution of the $S(H)$ curves is much more complex in the case of d_3. As in the case of d_5, the position of the maximum follows $\mu_0 H_c(T)$ but the maximum itself does not vary in a monotonous way with the temperature and a decrease in the width of $S(H)$ is observed beyond 100 K, as shown in figure 7(c). Such behavior contrasts with the constant width observed in the case of d_5. This clearly indicates the existence of two different regimes at low and high temperature. We will come back to this point in the following discussion.

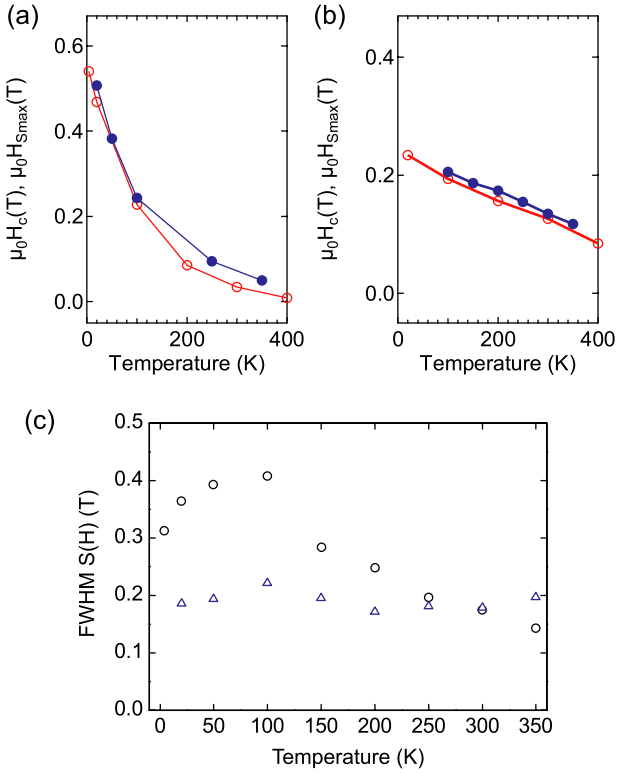

Figure 7. (a) Coercive field (circles) and field of maximal viscosity (disks) as a function of the temperature for d_3 (b) Same as (a) for d_5. (c) Full width at half maximum of $S(H)$ as a function of the temperature for d_3 (circles) and d_5 (triangles).

In what follows, we will label $S_{max}(T)$ the maximal value of the magnetic viscosity at a given temperature T. Information on the nature of the energy barriers can be obtained by analyzing the variation of $S_{max}(T)$. From $S_{max}(T)$, it is also possible to extract the variation of the activation volume $V^\star$ with the temperature using equation (7). In order to use this relation and deduce $V^\star$ values from the data, the irreversible part of the susceptibility, χ_{irr}, was determined from remanence magnetization loops [13]. The $S_{max}(T)$ and $V^\star(T)$ data obtained for d_3 and d_5 are plotted in figure 8.

We first discuss the results obtained for the d_5 nanowires assembly. As shown in figure 8(a), $S_{max}(T)$ varies linearly with the temperature. Such a linear variation is expected in the case of a temperature-independent energy barrier distribution, see equation (3). From the linear fit and using equation (4), it is also possible to extract the width of the distribution, ΔE_a. It is found that $\Delta E_a = 2$ eV. This width also corresponds to the highest value of the energy barrier present in the distribution in the framework of the rectangular approximation. Thus, the present value of ΔE_a is fully consistent with the mean value of $E_a = 1.6$ eV determined previously [8] by fitting the $\mu_0 H_c(T)$ variation with Sharrock's formula given by equation (9) [25].

The variation of $V^\star$ could also be reproduced in the framework of a thermally activated reversal of the magnetization. The data could be fitted quite satisfactorily using equation (10) with $m = 3/2$, yielding a $T^{1/3}$ dependence of $V^\star$, as shown in figure 8(b). In our previous study using static measurements [8], fitting the $\mu_0 H_c(T)$ variation with Sharrock's formula did not allow us to discriminate clearly between $m = 2$ and $m = 3/2$, both values giving comparable agreement of the fit with the data. In the present case, fitting $V^\star(T)$ with equation (10) and $m = 2$ (not shown) gives a much poorer agreement than $m = 3/2$. This 3/2 value is expected for systems with inhomogeneities and was also reported in previous studies of ferromagnetic nanowires grown in porous

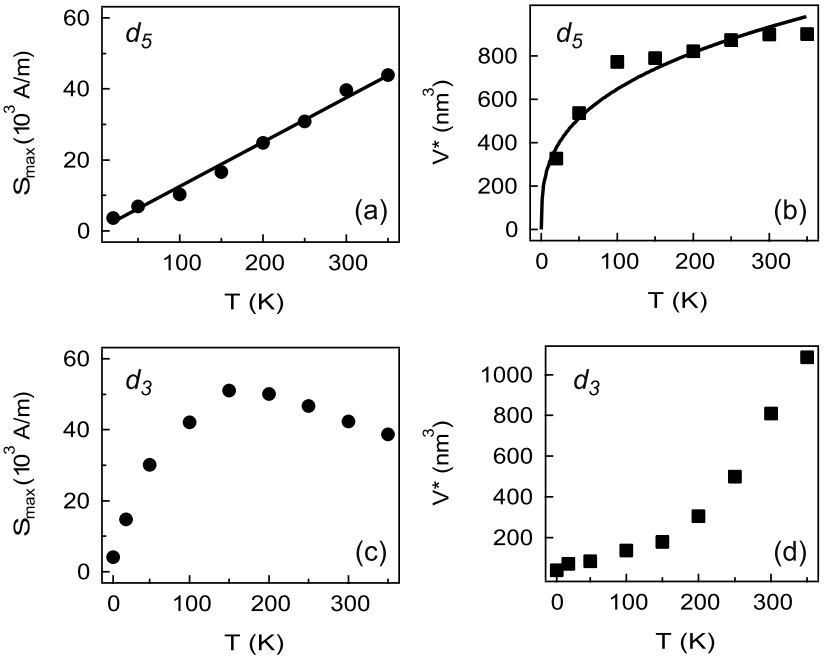

Figure 8. (a) Magnetic viscosity coefficient S_{max} of d_5 as a function of the temperature. The line is a linear fit. (b) Activation volume $V^\star$ of d_5 as a function of the temperature. The line is a fit according to equation (10) with $m = 3/2$. (c) Magnetic viscosity coefficient S_{max} of d_3 as a function of the temperature. (d) Activation volume $V^\star$ of d_3 as a function of the temperature.

alumina templates [2, 26]. $V^\star$ is of the order of a few hundreds of nm^3, reaching 900 nm^3 at 300 K. Such values are also comparable to activation volumes previously reported. The fact that these volumes are smaller than the physical volume of a FNW indicates that the reversal is localized.

Summarizing the results obtained for the d_5 FNWs assembly, we observe the typical behavior expected for a system with thermally activated localized reversal and no dependence on the temperature of the energy barriers. This indicates that the barrier is related to magnetostatic terms, i.e. to the resultant from shape anisotropy (favoring an easy axis along the wires' axis) and dipolar coupling among FNWs (this antiferromagnetic coupling acts against shape anisotropy). Here shape dominates over dipolar interactions and the resulting easy axis lies along the wires' axis. These two magnetostatic contributions to the anisotropy can be merged in a single magnetostatic contribution $\frac{\mu_0}{4}M_s^2(1-3P)$, where P is the porosity (volume fraction occupied by the wires) [27, 28]. In the temperature range under study, M_s is fairly constant and, thus, the anisotropy of the system does not depend on the temperature.

We now turn to the results obtained on the d_3 assembly. The overall behavior is strikingly dissimilar, both for the viscosity and for the activation volume, when compared to the case of d_5. Obviously, $S_{\max}(T)$ does not vary linearly and is not even monotonous with the temperature: it decreases beyond 150 K. The variation of $V^\star$ cannot be described by equation (10), neither with $m = 2$ nor with $m = 3/2$. The values of $V^\star$ indicate that the reversal process is localized in d_3. Beyond 150 K, $V^\star$ starts to increase much more rapidly than what is expected from a $T^{1/3}$ dependence. There is thus a progressive weakening of the localization of the reversal as the temperature increases. The reversal cannot be described with a temperature-independent distribution of energy barriers. The decrease of the width of $S(H)$ with increasing temperature indicates a clear change in this distribution. Such a distribution is closely related to inhomogeneities in system. In the present case, we argue that the internal structure of the wires is the key to explaining the observed changes in the variation of S and $V^\star$ with the temperature.

6. Discussion

It is possible to rationalize the observed behavior and to explain the weakening of the localization of the reversal by considering wires made of hcp Co grains having their c axis strongly misaligned with respect to the axis of the wires, as illustrated in figure 9. As the uniaxial magnetocrystalline anisotropy of hcp Co, $K_{1,u}$, is of the same order of magnitude as the shape anisotropy of the wires, a distribution of hcp grains, with varying size and/or orientation, within the wires will lead to a broad energy barrier distribution. This is due to the competition of shape and magnetocrystalline anisotropies that will induce local variation of the anisotropy along the axis of the wires, as depicted in figure 9. This is coherent with the large width of $S(H)$ at low temperatures.

Local variation of the anisotropy tends to induce the localization of the reversal in nanowires [12]. Therefore, in

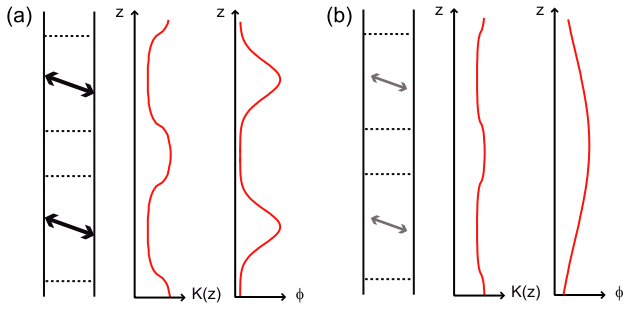

Figure 9. (a) Schematic illustration of the effect of local competition between magnetocrystalline and shape anisotropies, leading to a localized reversal of the magnetization. $K(z)$ is the local anisotropy constant, which is reduced in grains having their c axis oriented along the direction indicated by the double arrows. ϕ is the angle between the local magnetization and the axis of the wire. (b) Same as (a) with a reduced value of the magnetocrystalline anisotropy.

wires having an inner structure such as the one depicted schematically in figure 9, such a localization of the reversal process is expected. Again this is coherent with the reduced values of $V^\star$ at low temperature. As the temperature increases, $K_{1,u}$ drops [29]. This has two consequences: the width of $P(E_a)$ decreases (the system can be considered as more homogeneous than at low temperature from a magnetic point of view) and the local variation of the anisotropy is damped. A smaller variation of the anisotropy then leads to a weakening of the localization of the reversal, as illustrated in figure 9(b). Thus, the observed increase of $V^\star$ at higher temperatures may be a consequence of a weakening of the localization effects because of the drop of $K_{1,u}$.

The possible origin of the strikingly dissimilar behavior observed for d_3 and d_5 may lie in the internal structure of the wires. Small grain size and large stacking faults density in d_5 leads to a polycrystalline behavior in the sense that the contribution of $K_{1,u}$ is averaged to zero. In contrast, our HRTEM study shows that the wires in d_3 are composed of hcp grains that are larger than in d_5 and have non-random orientations. This leads to a non-zero effective magnetocrystalline contribution to the total anisotropy. Given the 54.7° angle between the c-axis and the wires axis, this contribution will compete with the magnetostatic one and will thus induce a local weakening of the anisotropy, as illustrated in figure 9. Because $K_{1,u}$ is temperature dependent and drops beyond 150 K, this weakening will be less and less pronounced as the temperature increases, leading to a progressive delocalization of the reversal.

To conclude, we have studied the grain structure and the magnetic relaxation in self-assembled Co nanowires with 3 and 5 nm diameters. In the 5 nm diameter wires assembly, the temperature dependences of the magnetic viscosity and of the activation volume could be fitted in the framework of a mechanism of thermally activated reversal of the magnetization using equations derived for a temperature-independent energy barrier distribution. This is consistent with the structure of the wires that leads to a vanishing magnetocrystalline anisotropy contribution and thus to a temperature-independent energy barrier distribution in the

range studied. Such a temperature-independent model fails to describe the data obtained from relaxation measurements performed on the 3 nm nanowires assembly. In the latter case, a peculiar behavior is observed with a decrease in the width of $S(H)$ and a strong increase of $V^{\star}$ beyond 150 K. These results, and especially this progressive delocalization of the reversal process, can be correlated with the internal structure of the 3 nm wires, composed of hcp grains having hexagonal axis oriented along non-random directions, strongly misoriented with respect to the wires axis. This leads to an effective temperature-dependent magnetocrystalline anisotropy that competes with the magnetostatic term.

Acknowledgments

We thank V H Etgens for stimulating discussions and continuous support. We thank F Breton for his skillful help and the development of the control software of our PLD apparatus. We thank B Capelle and J-M Guigner, IMPMC, CNRS-UPMC, for access to the TEM facilities. This work has been supported by ANR, grant ANR-2011-BS04-007-01, and by the Region Ile-de-France in the framework of C'Nano IdF. C'Nano IdF is the nanoscience competence center of Paris Region, supported by CNRS, CEA, MESR and Region Ile-de-France. PS and AJAO acknowledge support from FAPESP (grants 2007/08649-5 and 2008/10276-5) and CNPq. FV thanks FAPESP (grant 2011/03497-8). JM acknowledges Mairie de Paris for the awarded fellowship during his stay at INSP in Paris.

References

[1] Fert A and Piraux L 1999 *J. Magn. Magn. Mater.* **200** 338
[2] Sellmyer D J, Zheng M and Skomski R 2001 *J. Phys.: Condens. Matter* **13** R433
[3] Sun L, Hao Y, Chien C-L and Searson P C 2005 *IBM J. Res. Dev.* **49** 79
[4] Paulus P M, Luis F, Kröll M, Schmid G and de Jongh L J 2001 *J. Magn. Magn. Mater.* **224** 180
[5] Mohaddes-Ardabili L *et al* 2004 *Nature Mater.* **3** 533
[6] Zheng H, Wang J, Mohaddes-Ardabili L, Wuttig M, Salamanca-Riba L, Schlom D G and Ramesh R 2004 *Appl. Phys. Lett.* **85** 2035
[7] Vidal F, Zheng Y, Milano J, Demaille D, Schio P, Fonda E and Vodungbo B 2009 *Appl. Phys. Lett.* **95** 152510
[8] Schio P, Vidal F, Zheng Y, Milano J, Fonda E, Demaille D, Vodungbo B, Varalda J, de Oliveira A J A and Etgens V H 2010 *Phys. Rev.* B **82** 094436
[9] Vidal F, Schio P, Keller N, Zheng Y, Demaille D, Bonilla F J, Milano J and de Oliveira A J A 2012 *J. Phys. B: Condens. Matter* **407** 3070
[10] Vidal F, Zheng Y, Schio P, Bonilla F J, Barturen M, Milano J, Demaille D, Fonda E, de Oliveira A J A and Etgens V H 2012 *Phys. Rev. Lett.* **109** 117205
[11] Zheng Y, Vodungbo B, Vidal F, Selmane M and Demaille D 2008 *J. Cryst. Growth* **310** 3380
[12] Skomski R 2003 *J. Phys.: Condens. Matter* **15** R841
[13] Gaunt P 1986 *J. Appl. Phys.* **59** 4129
[14] Wegrowe J-E, Meier J P, Doudin B, Ansermet J-Ph, Wernsdorfer W, Barbara B, Coffey W T, Kalmykov Y P and Déjardin J L 1997 *Europhys. Lett.* **38** 329
[15] Gao J-H, Zhan Q-F, He W, Sun D-L and Cheng Z H 2006 *J. Magn. Magn. Mater.* **305** 365
[16] Gao J-H, Sun D-L, Zhan Q-F, He W and Cheng Z H 2007 *Phys. Rev.* B **75** 064421
[17] Maurer T, Zighem F, Ott F, Chaboussant G, André G, Soumare Y, Piquemal J-Y, Viau G and Gatel C 2009 *Phys. Rev.* B **80** 064427
[18] Zhang G, Wu Z Y, Li A, Wang Y, Zhang J, Abbas M I, Hu R, Ni X, Tong Y and Hwu Y 2004 *Phys. Rev.* B **69** 115405
[19] Miyawaki J, Matsumura D, Nojima A, Yokoyama T and Ohta T 2007 *Surf. Sci.* **601** 95
[20] Néel L 1949 *Ann. Geophys. (CNRS)* **5** 99
[21] Brown W 1963 *Phys. Rev.* **130** 1677
[22] Street R and Wooley J C 1949 *Proc. Phys. Soc.* A **62** 562
[23] Stoner E C and Wohlfarth E P 1948 *Phil. Trans. R. Soc.* A **240** 599
[24] Fruchart O and Thiaville A 2005 *C. R. Physique* **6** 921
[25] Sharrock M P 1994 *J. Appl. Phys.* **76** 6413
[26] Zeng H, Skomski R, Menon L, Liu Y, Bandyopadhyay S and Sellmyer D J 2002 *Phys. Rev.* B **65** 134426
[27] Encinas-Oropesa A, Demand M, Piraux L, Huynen I and Ebels U 2001 *Phys. Rev.* B **63** 104415
[28] Vega V, Böhnert T, Martens S, Waleczek M, Montero-Moreno J M, Görlitz D, Prida V M and Nielsch K 2012 *Nanotechnology* **23** 465709
[29] Ono F and Maeta H 1989 *Physica* B **161** 134